

Ultrafine Cu-Pd bimetallic clusters enhance asymmetric electron distribution to boost C-C coupling in photothermal CO₂-to-ethanol conversion

Fu Li, Jingnan Yang, Xiaomei Zhou, Fei Han, Qian Huo, Qingxin Guan*, Wei Li*

College of Chemistry, State Key Laboratory of Elemento-Organic Chemistry, Key Laboratory of Advanced Energy Materials Chemistry (Ministry of Education), Nankai University, Tianjin 300071, China

ARTICLE INFO

Keywords:
CO₂ reduction
Photothermal
Asymmetric electron distribution
C-C coupling
Ethanol

ABSTRACT

Converting CO₂ to ethanol through photothermal catalysis faces significant challenges due to it involves multi-electron reduction and kinetically sluggish C-C coupling process. Here, copper and a minor quantity of palladium are encapsulated within the cage of UiO-66 using a dual-solvent-sonication method to form ultrafine Cu₂O/Cu-Pd clusters. The Cu-Cu₂O serves as an electron center to enhance CO₂ uptake and activation, while the incorporation of Pd accelerates H₂ activation. Due to differences in electronegativity, electrons tend to transfer from Cu to Pd, which reduces the electrostatic repulsion between intermediates and facilitates the coupling of *CO and *CHO. The photothermal ethanol yield of Cu₆Pd@UiO-66 reached 1077.69 μmol·g⁻¹·mL⁻¹ with a selectivity of 94.62%, representing an 11.64-fold increase over the non-illumination, and a 3.11-fold enhancement compared with Cu₆@UiO-66. This study offers evidence supporting the promotion of C-C coupling through an asymmetric electron distribution, potentially advancing the conversion of CO₂ to liquid products.

1. Introduction

Ethanol, as an important small molecule organic compound, is often used in food processing, healthcare, and chemical production. Therefore, the preparation of ethanol with high selectivity and high yield is particularly important for people's lives. Carbon dioxide (CO₂), as a key gas to alleviate the greenhouse effect, can be used as a raw material for the preparation of ethanol, which can not only solve energy problems but also environmental problems [1]. But CO₂ is a thermodynamically stable and chemically inert molecule, therefore activating CO₂ requires additional energy input. As we all know, CO₂ hydrogenation to ethanol is an exothermic process. The higher temperature will accelerate the reverse water-gas shift reaction, which is not conducive to the production of ethanol. Therefore, the appropriate means of energy injection play an important role in minimizing by-products and reducing energy consumption. Photocatalytic and electrocatalytic reduction CO₂ are limited due to the low efficiency, while thermal catalysis is limited due to high energy consumption. While, photothermal catalysis emerges as a synergistic combination of photocatalytic and thermal catalytic processes, utilizing photons to generate active electron-hole pairs and thermal energy to promote chemical bond rearrangement, achieving

higher reaction efficiency and better product selectivity. However, achieving efficient photothermal CO₂ remains a complex task. It requires the development of robust catalysts that are stable under photothermal conditions, optimization of reaction conditions to maximize yield and selectivity, and the design of systems that can effectively capture and utilize sunlight [2–5].

Currently, Cu-based catalysts are widely considered as the most promising candidates for electrocatalytic, photocatalytic, and photothermal catalytic CO₂ to ethanol. Guo et al. reported a photocatalyst with atomically dispersed InCu on polycarbodimide (PCN), wherein light promotes electron generation from PCN and transfer to In-Cu sites, accelerating carrier separation. Meanwhile, the In sites transfer electrons to Cu sites using Cu-N-In as a bridge. The bimetallic site provides adsorption sites for intermediate *CO, and the electron-rich Cu site also reduces the coupling barrier of C-C. The yield of ethanol by photocatalytic process was 28.5 μmol·g⁻¹·h⁻¹ with a selectivity of up to 92% [6]. However, the yield of ethanol is still too low. Li et al. reported a Cu₂O/g-C₃N₄ catalyst with a heterojunction structure prepared by hydrothermal method. With the assistance of ionic liquid, the yield of CO₂ photothermal preparation of ethanol reached 0.71 mmol·g⁻¹·mL⁻¹. However, the stability of Cu⁺ and the yield issues are still difficult to

* Corresponding authors.

E-mail addresses: qingxinguan@nankai.edu.cn (Q. Guan), weili@nankai.edu.cn (W. Li).



solve [7]. Bai et al. [8] added Cu to Pd NPs to form Pd_2Cu NPs and loaded them on TiO_2 (P25) carriers to participate in CO_2 hydrogenation. The authors proposed that the alternating double metal arrangement improves the bridge-bonded $^*\text{CO}$ species on Pd, which promotes the ethanol yield and selectivity. However, noble metals are still the main active component, which results in high cost. At the same time, the harsh reaction conditions also hinder further development and research of this technology.

Metal Organic Framework (MOF), as a semiconductor hybrid organic-inorganic material with a tunable structure, can provide a relatively stable environment and the independent space to ensure the stability of the metal site. Therefore, MOFs are expected to be utilized for photothermal catalysis of CO_2 hydrogenation to ethanol and to promote a deeper understanding of the structure-activity relationship [9]. Numerous studies have shown that Zr-based carriers have superior CO_2 adsorption properties [10–19]. Additionally, UiO-66 is one of the most extensively studied Zr-MOFs. UiO-66 is one of the most perfect CO_2 hydrogenation carriers because of its cage-like structure, which provides a secure and isolated environment that guarantees the stability of the metal sites, boosting their dispersion and restricting their size [20–23].

Up to now, the research on the photothermal preparation of ethanol from metal-loaded M@UiO-66 has not been reported. According to the report by Zhu et al., the missing linkers in UiO-66 were occupied by Cu, which could maximize the interfacial ratio of metallic Cu to ZrO_2 nodes, resulting in a high CO_2 adsorption capacity and high activity [24]. However, the main product obtained was methanol. Zeng et al. reported a $\text{Cu}^{II}(\text{H}_3\text{PO}_4)_y$ @Ru-UiO hybrid that achieved CO_2 photothermal catalytic ethanol using electrons transfer between $[\text{Ru}(\text{bpy})_3]^{2+}$ and $\text{Cu}^{\delta+}$ under light, with a yield of $9650 \mu\text{mol}\cdot\text{g}_{\text{Cu}}^{-1}\cdot\text{h}^{-1}$ [18]. Zhao et al. engineered a heterometallic Sn…Cu bimetallic catalyst, composed of SnN_2O_2 and CuN_4 sites interlinked via $\mu\text{-N}$ atoms. The SnN_2O_2 sites exhibit a strong affinity for oxygen, which facilitate the formation of $^*\text{OCH}_2$, while the Cu sites are beneficial for $^*\text{CO}$ adsorption, thus enhancing C-C coupling [25]. Zhu et al. induced asymmetric distribution of electrons in adjacent C1 through Zn-O-Ge to promoting C-C coupling [26]. Liu et al. confirmed that surface segregation caused by CoCu promotes the breaking of C-O bonds and the formation of $^*\text{CH}_2\text{O}$, which is a key step in the production of ethanol [27]. It seems that catalysts with single metal sites are difficult to achieve the conversion of CO_2 to ethanol, as this requires multiple coupled proton and electrons transfer processes. The asymmetric distribution of electrons on the C1 intermediates

brought about by the bimetallic sites can help to break the phase-meeting repulsion between the intermediates and promote C-C coupling. Therefore, dual metal sites have become an important strategy for improving the yield and selectivity of ethanol.

In this work, UiO-66 with abundant defects was synthesized using acetic acid as a moderator. The precursor was synthesized by dual-solvent sonication, and H_2 pyrolysis treatment resulted in the formation of catalysts with ultrafine $\text{Cu}_2\text{O}/\text{Cu-Pd}$ clusters embedded in UiO-66 (Scheme 1). The $\text{Cu}_6\text{Pd}@\text{UiO-66}$ exhibited the highest photothermal ethanol yield as well as selectivity, compared to $\text{Cu}_6@\text{UiO-66}$. $\text{Cu}_2\text{O}/\text{Cu}$ enhanced the ability to collect light and acted as an electron center to promote CO_2 hydrogenation, while the introduction of Pd facilitated the photogenerated charge generation and reduced the photogenerated electron interfacial transfer impedance, accelerating CO_2 hydrogenation. The active site-wrapped structure ensures the stability of the catalyst during the photothermal reduction of CO_2 , while the asymmetric distribution of the active sites promotes C-C coupling, affecting the hydrogenation reaction path and selectivity. This structure provides ideas for stabilizing the unsaturated valence state of Cu, while this catalyst with dual active sites provides potential for the preparation of high value-added products such as C_2+ from CO_2 hydrogenation.

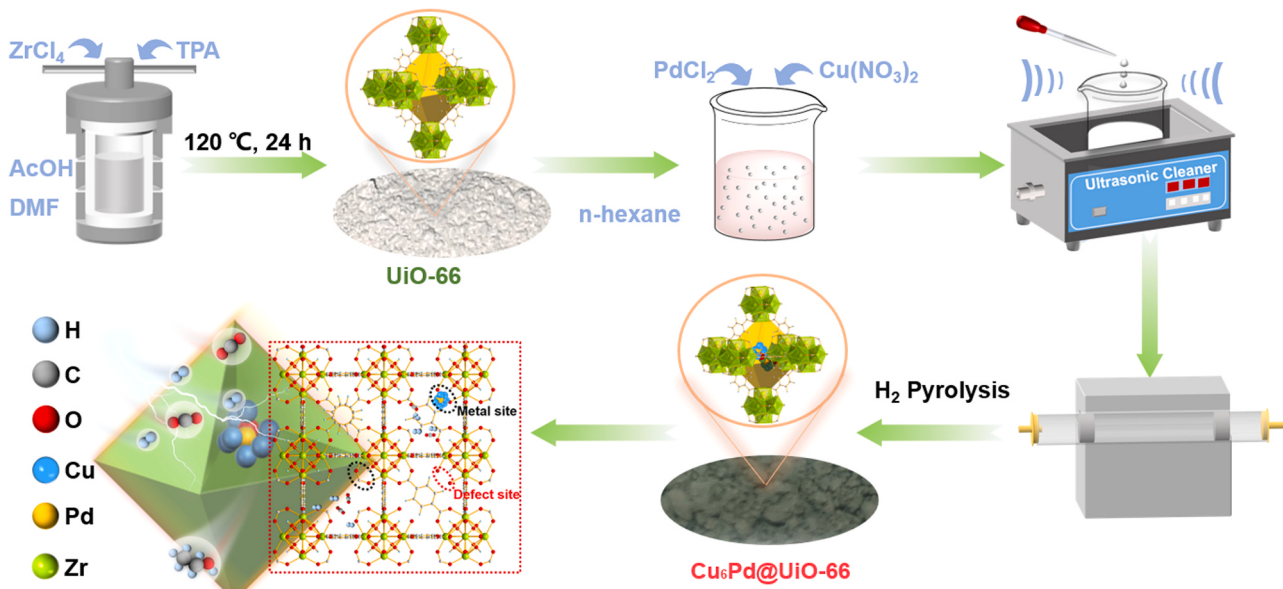
2. Experimental section

2.1. Chemicals

Acetic acid (99.5%), Terephthalic acid (95%), N,N-Methylmethylamine (95%), and Hexane (99%) were obtained from Aladdin. Zirconium chloride (98%), Copper(ii) nitrate hydrate ($\geq 99\%$), Palladium chloride (98%), and Triethanolamine (99%) were purchased from Macklin. All of them were directly used without further purification in our experiments.

2.2. Preparation of catalysts

UiO-66 was synthesized by solvothermal method, reported by Ling et al. [16]. Typically, 466 mg zirconium tetrachloride, 332 mg terephthalic acid, and 15 mL acetic acid were dissolved in 50 mL of DMF. Then, the mixed solution was transferred to polytetrafluoroethylene lining for solvothermal treatment at 120 °C for 24 h. After that, the products were ripened by centrifugation and washing alternately with



Scheme 1. Schematic illustration of the synthesis process employed in producing $\text{Cu}_6\text{Pd}@\text{UiO-66}$.

DMF and acetone several times. Finally, the obtained products were put into a vacuum drying oven and dried at 60 °C for 24 h.

$\text{Cu}_x\text{Pd}@\text{UiO-66}$ was synthesized via a dual-solvent-sonication method. Specifically, 1 g of UiO-66 was added into 50 mL n-hexane, and dispersed by ultrasonication for 30 min. Afterwards, 2 mL of a mixture of $\text{Cu}(\text{NO}_3)_2 \cdot 3 \text{H}_2\text{O}$ and PdCl_2 in varying concentrations was gradually added dropwise to the above solution, following a 3 h sonication. After that, the metal-loaded products were collected by centrifugation, washing with acetone for several times to remove the residual reactants, and vacuum drying at 60 °C for 24 h. Finally, the harvested products were pyrolyzed in a stream of H_2 (30 $\text{mL}\cdot\text{min}^{-1}$) at 200 °C for 4 h to obtain $\text{Cu}_x\text{Pd}@\text{UiO-66}$. The Cu/Pd molar ratios were changed (0.5, 2, 6, and 8) to optimize the activity of the resultant catalysts (Table S1). For comparison, the $\text{Cu}_x@\text{UiO-66}$ catalyst was also prepared with identical procedures as above except that without PdCl_2 was added.

2.3. Photothermal catalytic performance of CO_2 hydrogenation

The photothermal CO_2 hydrogenation to ethanol was performed in a stainless autoclave reactor equipped with a sapphire window. In a typical experiment, 100 mg of catalyst, 24 mL of deionized water, and 1 mL of triethanolamine were added to the reactor, and the reactor was initially purged with CO_2 several times to remove the air from the reactor. The reactor was pressured with CO_2/H_2 mixed gases to 20 bar to drive the reaction at 180 °C for 5 h under light irradiation with a 300 W Xe lamp and magnetic stirring. After the reaction, the liquid product was tested by gas chromatography GC-2014. The yield and selective of ethanol were calculated by the following equations:

$$\text{Production rate} (\mu\text{mol}\cdot\text{g}^{-1}\cdot\text{h}^{-1}) = \frac{\text{M}_{\text{EtOH}} * V_{\text{aq}}}{t * m_{\text{cat}}} \quad (1)$$

$$\text{Selectivity} (\%) = \frac{12 * \text{M}_{\text{EtOH}}}{12 * \text{M}_{\text{EtOH}} + 6 * \text{M}_{\text{MeOH}}} \quad (2)$$

where M_{EtOH} and M_{MeOH} represent the yield of ethanol, t and m_{cat} represent the reaction time and mass of catalyst, respectively.

The band gaps of $\text{Cu}_6@\text{UiO-66}$ and $\text{Cu}_6\text{Pd}@\text{UiO-66}$ were calculated using Tauc plot method. The formula is as follows:

$$(\alpha h\vartheta)^{\frac{1}{m}} = A(h\vartheta - E_g) \quad (3)$$

where α represents the absorption coefficient, $h\vartheta$ is the photon energy, m is the power index, typically 1/2 for direct transitions or 2 for indirect transitions, A is a constant determined from the linear fit of the Tauc plot, and E_g is the bandgap energy.

3. Result and discussion

3.1. Catalyst preparation and characterization

Terephthalic acid is widely recognized as an effective cross-linking agent for the preparation of MOF materials [16]. Acetic acid can be used as a regulator to replace the coordination of terephthalic acid in the synthesis of UiO-66, resulting in coordination defects. Moreover, the carboxylic acid ligands possess excellent riveting metal effects. Additionally, the excess small molecules of carboxyl groups can be easily eluted from UiO-66. Based on this, UiO-66 was prepared by the acid-catalyzed reaction of terephthalic acid and ZrCl_4 in DMF at 120 °C for 24 h. Then, a double-solvent sonication method was used to encapsulate Cu and Pd into the cage structure of UiO-66. This method can accurately control the amount of metal loaded into the framework, maintain the crystal structure of UiO-66 from being damaged, and ensure the formation of CO_2 hydrogenation microenvironment. Meanwhile, the $\text{H}_2\text{-TPR}$ results (Figure S1) provide support for strong metal-support interaction and bimetallic interactions. The FT-IR spectra (Figure S2) show that the C=O bond still exists after UiO-66 was

reduced at 200 °C in H_2 for 4 h, but the C=O bond disappeared after loading metal, indicating that the cooperation between the metal and carboxyl group makes it easier to be reduced.

The porosities of UiO-66, $\text{Cu}_6@\text{UiO-66}$, and $\text{Cu}_6\text{Pd}@\text{UiO-66}$ were studied by N_2 adsorption-desorption curve measurements. All of them showed a microporous sorption isotherm. Compared with the UiO-66, the Brunauer-Emmett-Teller (BET) surface areas of $\text{Cu}_6@\text{UiO-66}$ and $\text{Cu}_6\text{Pd}@\text{UiO-66}$ decreased from $1461.8 \text{ m}^2\cdot\text{g}^{-1}$ to $1229.6 \text{ m}^2\cdot\text{g}^{-1}$ and $1179.9 \text{ m}^2\cdot\text{g}^{-1}$, respectively, while the pore volume decreased from $0.73 \text{ cm}^{-3}\cdot\text{g}_{\text{cat}}^{-1}$ to $0.65 \text{ cm}^{-3}\cdot\text{g}_{\text{cat}}^{-1}$ and $0.55 \text{ cm}^{-3}\cdot\text{g}_{\text{cat}}^{-1}$ (Figure S3 and Table S1). Meanwhile, the BET results show that the specific surface area and pore size decreased gradually with the increase of Cu proportion (Figure S3). The results indicate Cu^{2+} and Pd^{2+} successfully encapsulated into the pores of UiO-66. However, when the Cu loading reached 8%, there was a significant decrease in specific surface area and an increase in pore size (Table S1). This may be due to clogging caused by excessive metal loading, preventing more additional Cu^{2+} from entering the pores. On the other hand, the thermogravimetric test demonstrated the catalysts were relatively stable below 200 °C, which could ensure that the catalysts did not decompose during the CO_2 hydrogenation process (Figure S4).

XRD patterns (Fig. 1a) show that all of them maintained the crystal structure of UiO-66, and the strong diffraction peaks also indicate their excellent crystal structure. The diffraction peaks of Cu (PDF# 04-0836) overlap with that of UiO-66, making it difficult to confirm the valence of Cu and necessitating further characterizations. However, based on the results of XRD and BET, it can be inferred that the metal sites are uniform dispersed and have a small size. The TEM images (Fig. 1b and c) also reveal an overall clean surface without any noticeable metal particle agglomeration or segregation, suggesting the metal is well-dispersed in UiO-66. Further HRTEM images (Fig. 1f and j) and the corresponding EDX elemental mapping images (Fig. 1h and l) reveal that ultrafine Cu clusters and Cu-Pd clusters are uniformly distributed in UiO-66, but ultrafine Cu-Pd clusters show a slight aggregation. The average diameter of atomic cluster increases from 0.73 to 0.85 nm. Meanwhile, the aberration-corrected HAADF-STEM images also reveal that the average diameter of $\text{Cu}_6\text{Pd}@\text{UiO-66}$ has an increase compared with $\text{Cu}_6@\text{UiO-66}$ (Fig. 1g and k). This result confirms that the electrons transfer between Cu and Pd occurs, resulting in Cu gathering around the Pd and forming the atoms clusters, which changes the electron distribution of ultrafine Cu clusters.

To determine the electric state of metal and bimetallic synergistic effect, the XPS tests were performed. According to the Pd 3d XPS spectra (Fig. 2a), a negative shift of 0.33 eV is observed for the position of Pd^0 , indicating the electrons transfer from Cu to Pd. By comparing the Cu 2p XPS spectra and Cu LMM (Fig. 2b and c) of $\text{Cu}_6@\text{UiO-66}$ and $\text{Cu}_6\text{Pd}@\text{UiO-66}$ reveals that Cu species present in the forms of Cu^{2+} , Cu^+ , and Cu^0 . However, a decrease in the area of Cu^0 indicates electron redistribution after the introduction of Pd. Furthermore, the Zr 3d spectra present two different Zr species (Table S2): Zr-I (Fig. 2d light color) belong to the saturated coordination; Zr-II (Fig. 2d dark color) belong to Zr-OH according to the report by Xu et al. [13,20,28–30]. The Zr-OH species also could be confirmed by O 1 s XPS (Figure S6). The proportion of Zr-OH in $\text{Cu}_6\text{Pd}@\text{UiO-66}$ was higher than that of $\text{Cu}_6@\text{UiO-66}$ and $\text{Pd}@\text{UiO-66}$, which further indicates that the introduction of Pd breaks the electronic coordination environment of Cu species.

To further dissect the valence state of copper in $\text{Cu}_6@\text{UiO-66}$ and $\text{Cu}_6\text{Pd}@\text{UiO-66}$, X-ray absorption spectroscopy (XAS) was conducted. In the XANES spectrum (Fig. 2e), there is a distinct feature at around 8980 eV, which is attributed to the pre-edge peak of Cu. This peak is sensitive to the local electronic structure around the absorbing atom and also can provide insights into the oxidation state and coordination number of copper. By comparing the XANES spectra of $\text{Cu}_6@\text{UiO-66}$ and $\text{Cu}_6\text{Pd}@\text{UiO-66}$ with the reference Cu foil, it should be noted that the pre-edge peaks of $\text{Cu}_6@\text{UiO-66}$ and $\text{Cu}_6\text{Pd}@\text{UiO-66}$ are shifted to higher energies, which suggests that the Cu species have higher valence states.

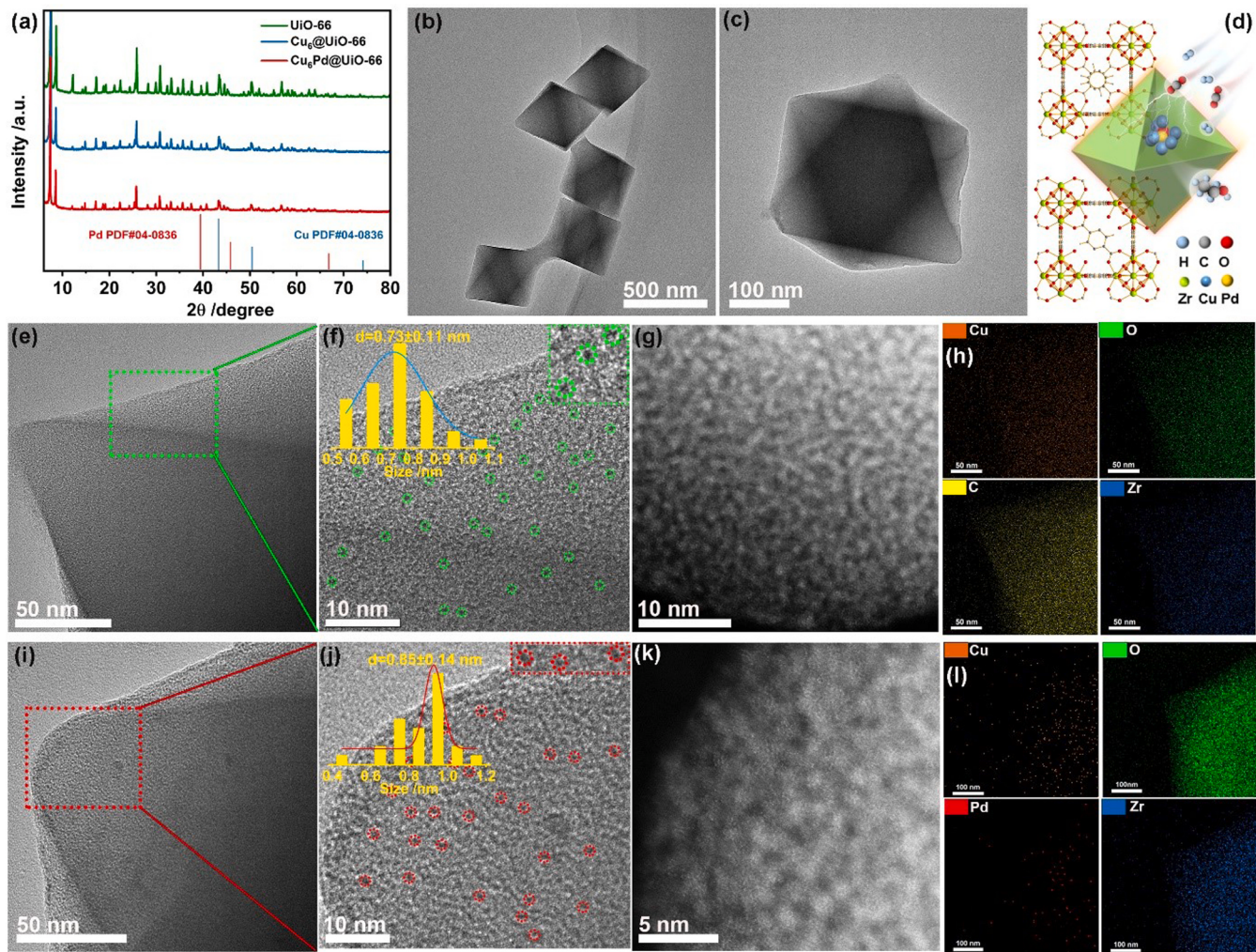


Fig. 1. (a) XRD patterns of UiO-66, Cu₆@UiO-66, and Cu₆Pd@UiO-66; (b, c) TEM images of UiO-66 and Cu₆@UiO-66; (d) Scheme of Cu₆Pd@UiO-66 catalyzed CO₂ hydrogenation; (e-h) HRTEM, HAADF-STEM images and elemental mappings images of Cu₆@UiO-66; (i-l) HRTEM, HAADF-STEM images and elemental mappings images of Cu₆Pd@UiO-66.

Additionally, the white line peak (Fig. 2e red dotted frame) of Cu₆@UiO-66 and Cu₆Pd@UiO-66 is located between the reference Cu₂O and Cu, which suggests that the major Cu species in Cu₆@UiO-66 and Cu₆Pd@UiO-66 exist as a mixture of Cu⁰ and Cu⁺. Fig. 2f illustrates the EXAFS spectra of Cu₆@UiO-66 and Cu₆Pd@UiO-66. The R-space positions of Cu-Cu peaks are between 2.23 and 2.67 Å in Cu foil, Cu₂O, and CuO. In contrast, the Cu-O peaks of Cu₂O and CuO are around at 1.48 Å and 1.56 Å, respectively. For Cu₆@UiO-66, the peak at 2.22 Å corresponds to the Cu-Cu bond of Cu, while the peak at 1.49 Å corresponds to the Cu-O first coordination shell of Cu₂O. The absence of second coordination shell of Cu₂O suggests that the size of Cu is small and uniformly dispersed. For Cu₆Pd@UiO-66, the peak of Cu-O at 1.52 Å is longer, which indicate that the addition of Pd affects the Cu-O bonding, further demonstrating Pd affects the electric distribution of Cu species.

To gain a deeper insight of the electrons active sites of the synthesized catalysts, in situ DRIFTS using CO as a probe molecule (CO-DRIFTS) was conducted on the UiO-66, Cu₆@UiO-66, and Cu₆Pd@UiO-66 (Fig. 2h-j). According to the reported [31–34], the $\nu(\text{CO})$ band above 2000 cm⁻¹ is attributed to terminal, monocoordinated or linearly bonded carbon monoxide. As shown in Fig. 2h, the peaks at 2174 and 2116 cm⁻¹ are assigned to the CO linear adsorption of UiO-66. However, after purging with Ar, these peaks disappeared, indicating a weak physical adsorption between CO and UiO-66. For the spectra of Cu₆@UiO-66 (Fig. 2i), besides the peaks at 2174 and 2116 cm⁻¹, a new

peak at 2101 cm⁻¹ appeared due to the introduction of Cu species. Surprisingly, after purging with Ar, the peak was still retained 1/4 of their intensities, illustrating a strong chemical adsorption between CO and Cu₆@UiO-66. Lan et al. reported CO adsorption only occurred on mononuclear Cu sites (Cu^{δ+}-CO) for Cu-based catalysts [32,35]. Thus, the peak at 2101 cm⁻¹ is attributed to the interaction between Cu-Cu₂O and CO, indicating that Cu-Cu₂O is the electron density center of Cu₆@UiO-66. The same phenomenon occurred on Cu₆Pd@UiO-66 (Fig. 2j), but after purging with Ar, the intensity at 2101 cm⁻¹ decreased compared with that of Cu₆@UiO-66. We speculated it caused by the electrons transfer from Cu to Pd, which is in agreement with the conclusion of XPS and XAS.

3.2. Photothermal CO₂ reduction performance

To explore the effect of bimetallic electron transfer-induced electron asymmetric distribution on photothermal performance, the CO₂ hydrogenation reaction was conducted in a stainless autoclave reactor equipped with a sapphire window. The obtained liquid products were detected by ¹H NMR. The results showed that the liquid phase products were methanol and ethanol (results depicted in Figure S8). And the experiment using D₂O as solvent proved that H originates from the dissociation of H₂ by the catalysts (Figure S8). As shown in Fig. 3a, the ethanol yields of UiO-66, Pd@UiO-66, and Cu₆@UiO-66 were 12.45,

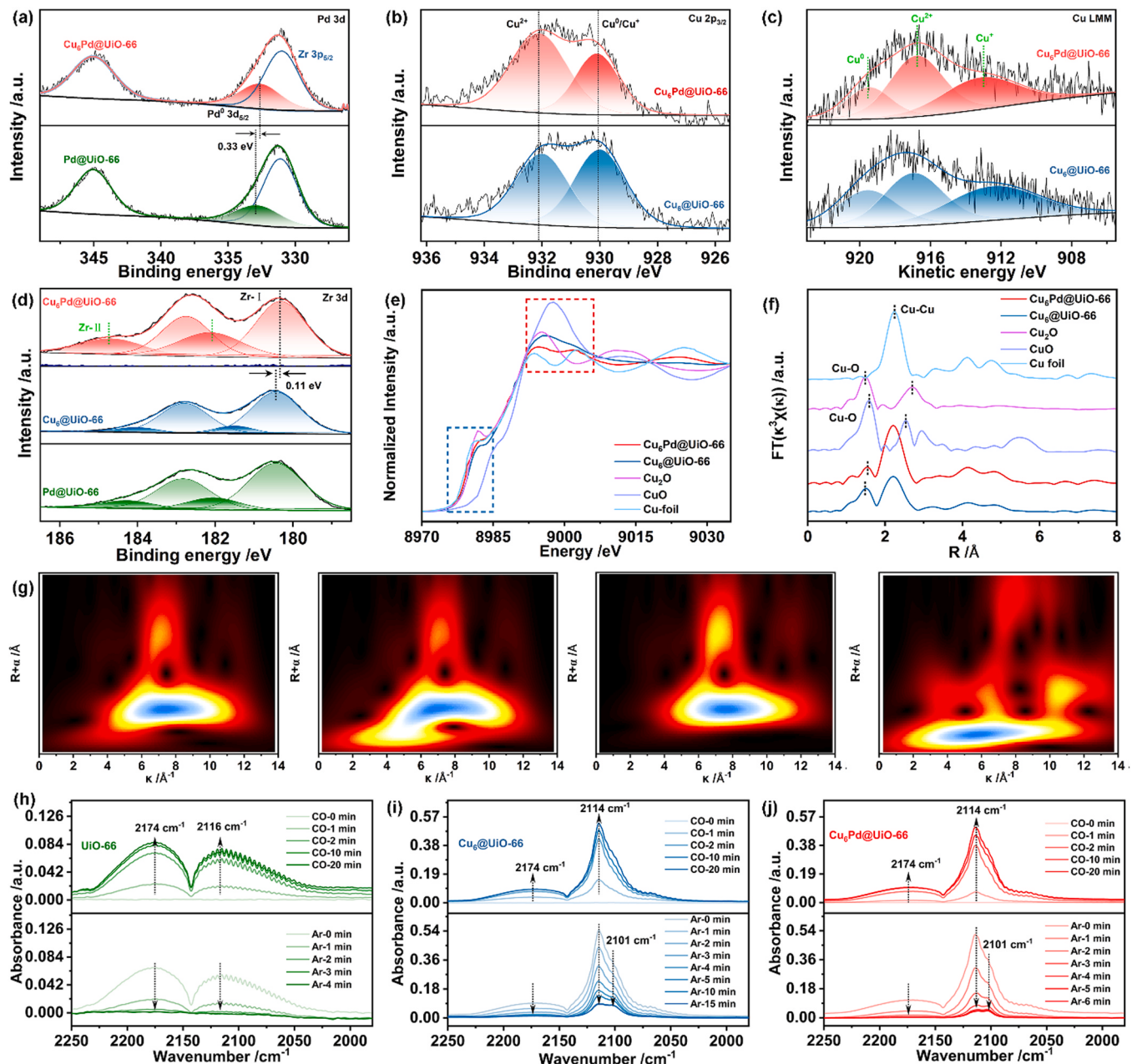


Fig. 2. (a) The Pd 3d XPS spectra of Pd@UiO-66 and Cu₆Pd@UiO-66; (b) The Cu 2p_{3/2} spectra of Cu₆@UiO-66 and Cu₆Pd@UiO-66; (c) Cu LMM Auger spectra of Pd@UiO-66 and Cu₆Pd@UiO-66; (d) The Zr 3d spectra of Pd@UiO-66, Cu₆@UiO-66, and Cu₆Pd@UiO-66; (e) XANES and (f) FT-EXAFS spectra at Cu edge of Cu₆@UiO-66, Cu₆Pd@UiO-66, Cu₂O, CuO, and Cu foil; (g) Wavelet transform contour plots of Cu foil, CuO, Cu₆@UiO-66 and Cu₆Pd@UiO-66 at Cu K-edge; (h-j) The in-situ CO-DRIFTS of UIO-66, Cu₆@UiO-66, and Cu₆Pd@UiO-66.

15.17, and 346.38 $\mu\text{mol}\cdot\text{g}_{\text{cat}}^{-1}\cdot\text{mL}^{-1}$, respectively. With the Cu/Pd ratio increased, the yield of ethanol increased from 26.03 $\mu\text{mol}\cdot\text{g}_{\text{cat}}^{-1}\cdot\text{mL}^{-1}$ to 1077.69 $\mu\text{mol}\cdot\text{g}_{\text{cat}}^{-1}\cdot\text{mL}^{-1}$, then decreased to 382.12 $\mu\text{mol}\cdot\text{g}_{\text{cat}}^{-1}\cdot\text{mL}^{-1}$. When the ratio of Cu/Pd reached 6:1, the catalytic efficiency reached an optimal level. As far as we know, the performance of Cu₆Pd@UiO-66 is more prominent (Fig. 3c and Table S4). Zeng et al.[18] have reported that the ethanol productivity rate was 9.650 mmol·g_{Cu}⁻¹·mL⁻¹ for Cu_{II}(H_xPO₄)_y@Ru·UiO, which is much lower than that of our Cu₆Pd@UiO-66 (22.22 mmol·g_{Cu}⁻¹·mL⁻¹). Additionally, the ethanol yield of Cu₆Pd@UiO-66 was 3.11 times that of Cu₆@UiO-66, while the selectivity was also increased to 94.62%, indicating that the introduction of Pd breaks the Cu-Cu₂O electron distribution and promotes C-C coupling.

To investigate whether the performance enhancement under illumination originates from the thermal effect produced by light, CO₂

hydrogenation performance tests were conducted under illumination or non-illumination at different temperatures. As shown in Fig. 3b, the reaction rates increase with increasing temperature. Additionally, the reaction rate with illumination was significantly higher than that of non-illumination. At 180 °C, the ethanol yield of Cu₆Pd@UiO-66 with light (1077.69 $\mu\text{mol}\cdot\text{g}_{\text{cat}}^{-1}\cdot\text{mL}^{-1}$) was 11.64 times higher than that of without light (92.57 $\mu\text{mol}\cdot\text{g}_{\text{cat}}^{-1}\cdot\text{mL}^{-1}$). Simultaneously, the reaction rate grows exponentially with light, while the reaction rate shows a linear increase trend without light. The result indicates that light irradiation does not enhance catalytic performance by generating heat, but breaks the photochemistry barrier of CO₂ hydrogenation.

The stability of Cu-based catalysts in oxidation-reduction reactions is a significant challenge. In this study, the experimental repeatability was tested under 180 °C and 2 MPa pressure (H₂/CO₂= 3/1) with

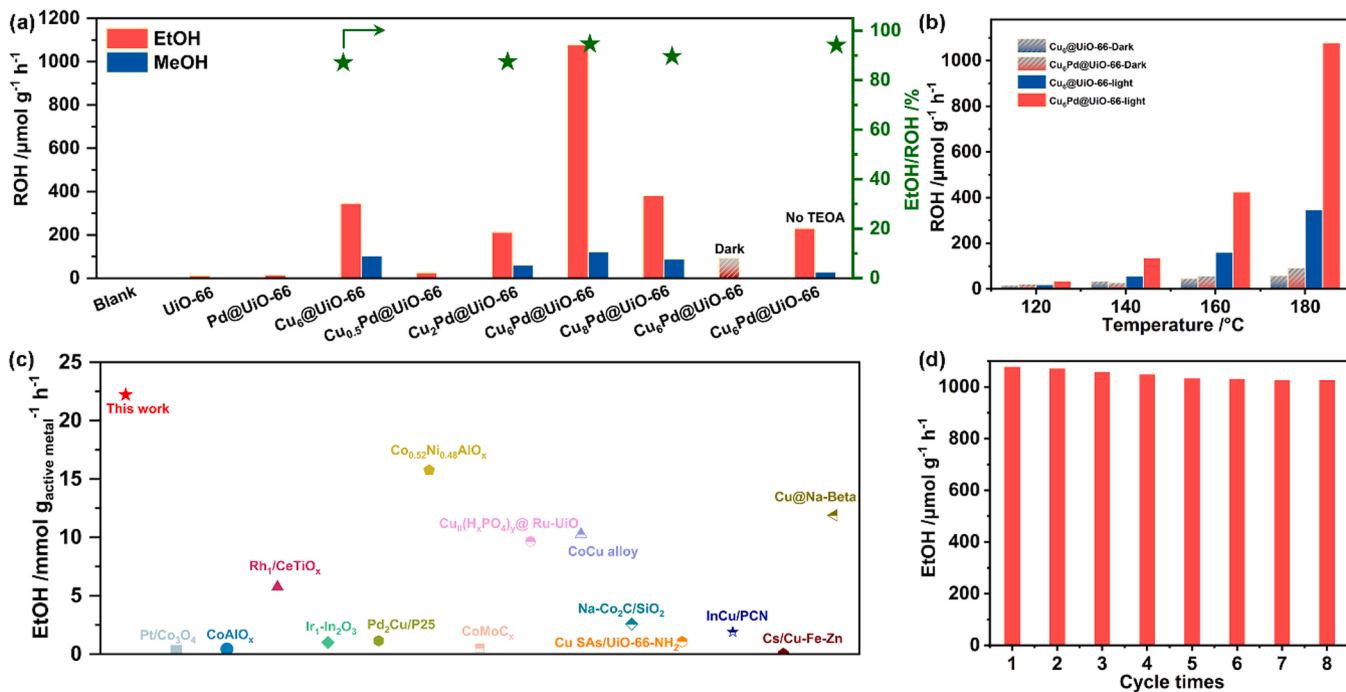


Fig. 3. (a) the ROH yield on different catalysts and (b) the ethanol yield of Cu₆@UiO-66 and Cu₆Pd@UiO-66 at different temperatures (100 mg catalyst, 24 mL H₂O, 1 mL TEOA, 0.5 MPa CO₂, and 1.5 MPa H₂); (c) The ethanol yield of Cu₆Pd@UiO-66 compared with those of most state-of-the-art catalysts [6,8,18,19,27,36–45]; (d) The recycling performance of Cu₆Pd@UiO-66 under light irradiation.

illumination. As shown in Fig. 3d, the catalytic performance remained relatively stable after eight cycles. And the XPS test was performed on the reused 8 times Cu₆Pd@UiO-66 (Figure S11). The Cu 2p_{3/2} spectra analysis reveal that the Cu species still exists in different valence states, indicating that the catalyst could maintain relatively stable in the reducing environment. It fully demonstrates that metal encapsulated into MOF can achieve the goal of stabilizing the valence state of metal and consequently maintain the catalytic activity.

3.3. Mechanism investigation

As discussed above, Cu₆Pd@UiO-66 exhibited outstanding photothermal catalysis for CO₂ hydrogenation to ethanol, which can be attributed to the strong interaction between metal and support. To identify the reason of higher photothermal activity, the absorption spectra were tested to determine the light-harvesting capacity of the catalysts. As shown in Fig. 4a, Cu₆Pd@UiO-66 exhibits the stronger light-harvesting than UiO-66 and Cu₆@UiO-66. And Cu₆@UiO-66 and Cu₆Pd@UiO-66 have an increasing trend over the entire ultraviolet-visible region compared with that of UiO-66. Additionally, a new spike appears at around 650 nm, which is attributed the characteristic absorption peak of Cu species. However, the characteristic absorption becomes faint for Cu₆Pd@UiO-66, indicating that the introduction of Pd break the electron distribution of Cu-Cu₂O. Simultaneously, to verify the correlation between light-harvesting capacity and the photothermal catalytic performance, the CO₂ hydrogenation of Cu₆Pd@UiO-66 was conducted under monochromatic irradiation. From Figure S10d, the yield of ethanol almost corresponds to the absorption of Cu₆Pd@UiO-66, which indicates metal species influence the performance of CO₂ hydrogenation by regulate the light-harvesting capacity of the catalysts.

Subsequently, the optical electronic structure has been investigated through band gap calculation and electrochemical tests. According to the Tacu plots (Eq. (3), Fig. 4b), the electronic band gap (E_g) of Cu₆@UiO-66 and Cu₆Pd@UiO-66 are 2.59 and 1.76 eV, respectively (Figure S12). And the VB-XPS reveal that the valence band (VB) positions are +1.42 and +1.85 eV, respectively. Thus, the conduction band

(CB) positions are -0.74 and -0.34 V. Furthermore, the Mott-Schottky curves also reveal the conduction-band potential of Cu₆@UiO-66 and Cu₆Pd@UiO-66 are -0.74 and -0.34 V (vs Ag/AgCl), respectively (Fig. 4c and d). The electronic structure is depicted in Fig. 4e. The narrowing of the band gap and the lowering of the CB position indicate that the illumination is more favorable for electrons to jump to the CB to participate in the catalytic reaction. The electrochemical impedance spectroscopy (EIS) technique was employed to study interfacial carrier transfer performance (Fig. 4f). It can be seen the solid-shaped arc radius is notably smaller than the hollow-shaped arc radius, implying that illumination on catalysts can expedite charge transfer. The ordering of arc radius is Cu₆Pd@UiO-66 < Cu₆@UiO-66 < UiO-66 (Fig. 4g), indicating that the loading of Cu and Pd can reduce the interface resistance of charge transfer. Electron paramagnetic resonance (EPR) studies were conducted on Cu₆@UiO-66 and Cu₆Pd@UiO-66 to detect photo-generated electrons transfer at the Cu and Pd sites [19,33,46]. As shown in Fig. 4h, Cu₆Pd@UiO-66 give a distinct signal at around g = 2.052 and the signal is dramatically intensified under light, due to the occurrence of photogeneration electrons transfer. On the other hands, the signal at g = 2.052 is enhanced meaning the more photo-generated electron. And the photocurrent of Cu₆Pd@UiO-66 is higher than those of UiO-66 and Cu₆@UiO-66 (Fig. 4i), also demonstrating the stronger photo-generated electron ability. In addition, based on the PDOS results (Figure S13), the d-band center of Cu in Cu₂O/CuPd is closer to the Fermi level compared with that of Cu₂O/Cu, indicating that Cu₂O/CuPd is more favorable for electron activation and transfer. Therefore, Cu₆Pd@UiO-66 generates more photogenerated carriers and faster photogenerated charge transfer than UiO-66 and Cu₆@UiO-66.

Fig. 5a-c exhibit the in-situ DRIFTS spectra to explore the change of surface chemical specials under illumination. Interestingly, the ligands of UiO-66 can release abundant -OH groups, which could form hydrogen bonds with intermediates such as *COOH, *CO, and *CHO. In the spectra recorded over Cu₆Pd@UiO-66, the peaks at 2797, 2763, 2640, and 1346 cm⁻¹ are attributed to *HCOO species [47]. The *HCOO species at 1346 cm⁻¹ showed increases initially, then decreases, and finally reaches a dynamic equilibrium (Fig. 5d). This phenomenon indicates

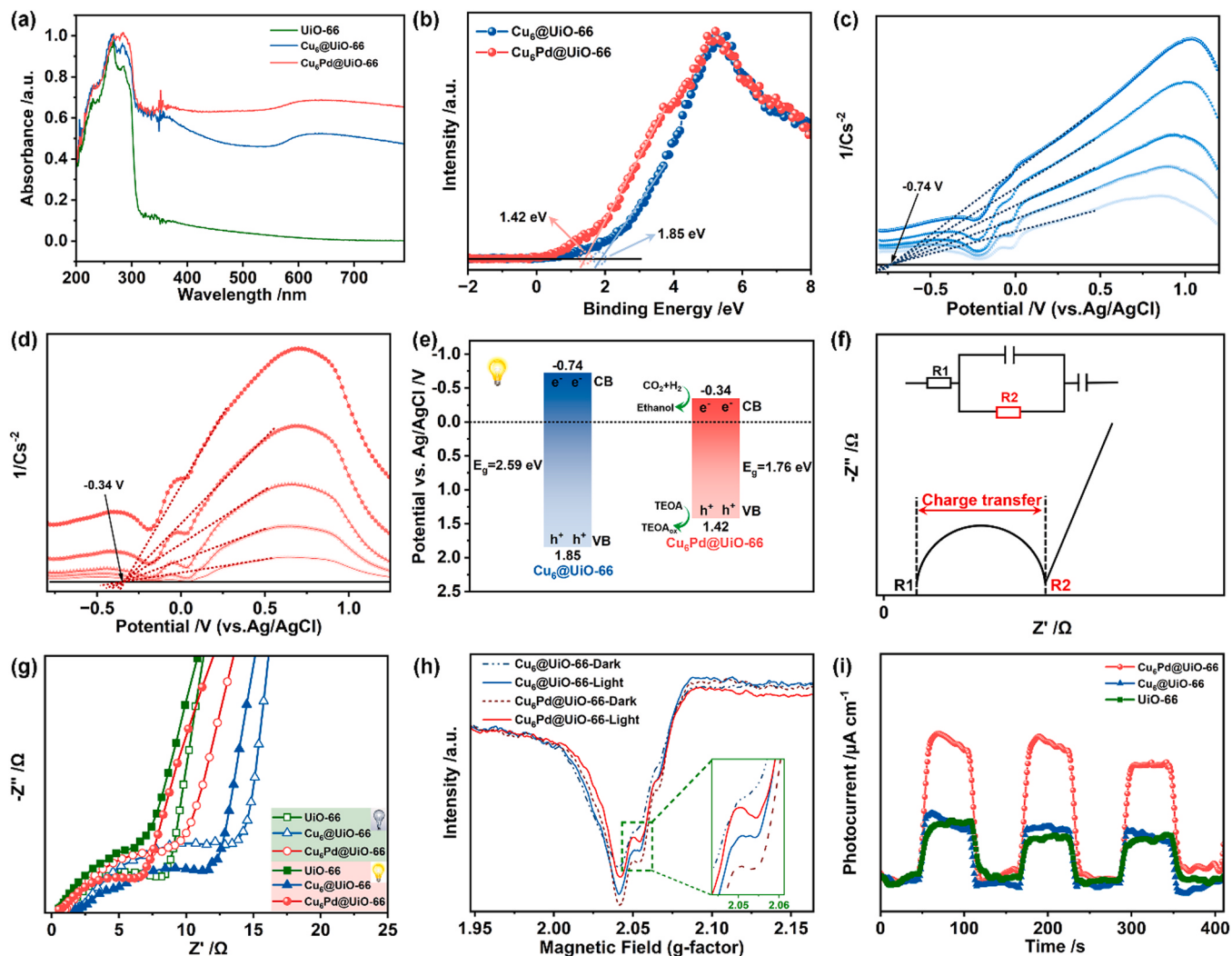


Fig. 4. (a) Absorption spectra and (b) VB-XPS of $\text{Cu}_6\text{@UIO-66}$ and $\text{Cu}_6\text{Pd}@\text{UIO-66}$; (c) and (d) MS plots of $\text{Cu}_6\text{@UIO-66}$ and $\text{Cu}_6\text{Pd}@\text{UIO-66}$; (e) The band structure of $\text{Cu}_6\text{@UIO-66}$ and $\text{Cu}_6\text{Pd}@\text{UIO-66}$; (f) and (g) EIS Nyquist plots of $\text{Cu}_6\text{@UIO-66}$ and $\text{Cu}_6\text{Pd}@\text{UIO-66}$; (h) Electron paramagnetic resonance (EPR) spectra of UIO-66 , $\text{Cu}_6\text{@UIO-66}$, and $\text{Cu}_6\text{Pd}@\text{UIO-66}$; (i) Photocurrent curves of UIO-66 , $\text{Cu}_6\text{@UIO-66}$, and $\text{Cu}_6\text{Pd}@\text{UIO-66}$.

that ${}^*\text{HCOO}$ is involved in the formation of ROH. On the other hand, the intensity of ${}^*\text{CHO}$ species was in fluctuation at 1715 cm^{-1} , indicating that ${}^*\text{CHO}$ species were constantly being generated and consumed. Interestingly, the intensity of ${}^*\text{CH}_3\text{O}$ species at 1019 cm^{-1} show an opposite trend, indicating that ${}^*\text{CHO}$ involved in the formation of methanol and is a rate-determining step for the generation of MeOH [24, 48]. The intensity of ${}^*\text{C}_2\text{H}_5\text{O}$ species at 2917 cm^{-1} showed an increase followed by a decrease [6, 49], which has the same trend with ${}^*\text{COOH}$ species at 2518 cm^{-1} . This result illustrate the production of ethanol is closely related to that of ${}^*\text{COOH}$. Based on the above results, there are two possible pathways for CO_2 hydrogenation to methanol and ethanol (formic acid route and reverse water-gas shift route).

DFT calculations further clarified the reaction pathway. According to CO_2 -TPD and H_2 -TPD result (Figure S14), CO_2 is first adsorbed at the open Zr-site and then transferred to the Cu-Cu₂O electron-rich active center, while the Pd site facilitates the dissociation of the active H^* to participate the subsequent hydrogenation process. As shown in Fig. 5e, the formation of ${}^*\text{HCOO}$ is exothermic with an energy barrier of 2.43 eV , while the formation of ${}^*\text{COOH}$ is endothermic with an energy barrier of 2.28 eV . Therefore, the formation of ${}^*\text{HCOO}$ is more favorable in thermodynamic with a lower energy barrier. However, the conversion of ${}^*\text{HCOOH}$ to CHO is an endothermic reaction with an energy barrier 3.70 eV , which would limit the reaction. In the $\text{Cu}_6\text{Pd}@\text{UIO-66}$ - ${}^*\text{COOH}$

process (Fig. 5e), the formation of ${}^*\text{CO}$, ${}^*\text{HCO}$, ${}^*\text{H}_3\text{CO}$, and H_3COH are all exothermic steps, which are both kinetically and thermodynamically favorable (Scheme 2). Meanwhile, Jiang reported that CO_2 hydrogenation to prepare methanol produces site at UIO-66 , the metal site mainly provides the active H [9]. We calculated the energy barriers of CO_2 hydrogenation by DFT pair on UIO-66 (Fig. 5f). The DFT calculation results show that the energy barrier of CO_2 to ${}^*\text{CO}_2$ on UIO-66 is reached -6.10 eV , which is difficult to occur.

The preparation of ethanol is a complex multi-intermediate step and the detailed reaction process is shown in Fig. 5g. The formation of ${}^*\text{COOH}$ (+2.28 eV) on $\text{Cu}_6\text{Pd}@\text{UIO-66}$ is an endothermic reaction that requires overcoming an energy barrier of 2.44 eV . Thus, it is a rate-determining step for the C1 intermediate species. The generation of ${}^*\text{HCOO}$ (-2.43 eV) is an exothermic reaction and a thermodynamically favorable process. However, ${}^*\text{HCOOH}$ (-4.95 eV) to ${}^*\text{HCO}$ (-1.26 eV) is an endothermic reaction, which becomes the rate determining step for the process of the ${}^*\text{HCOO}$ route. By comparison, ${}^*\text{COOH}$ pathway is more likely to be the route of CO_2 hydrogenation to ethanol. At the same time, we calculated whether methanol was involved in the formation of ethanol. The ${}^*\text{HCO}+{}^*\text{MeOH}$ pathway shows that the formation of ${}^*\text{HCOCH}_3$ is an endothermic reaction, making it theoretically difficult to occur. Interestingly, at the C-C coupling process of ${}^*\text{CO}+{}^*\text{CHO}$, the adsorption site is altered. Firstly, the ${}^*\text{CHO}$ tends to be adsorbed at Cu

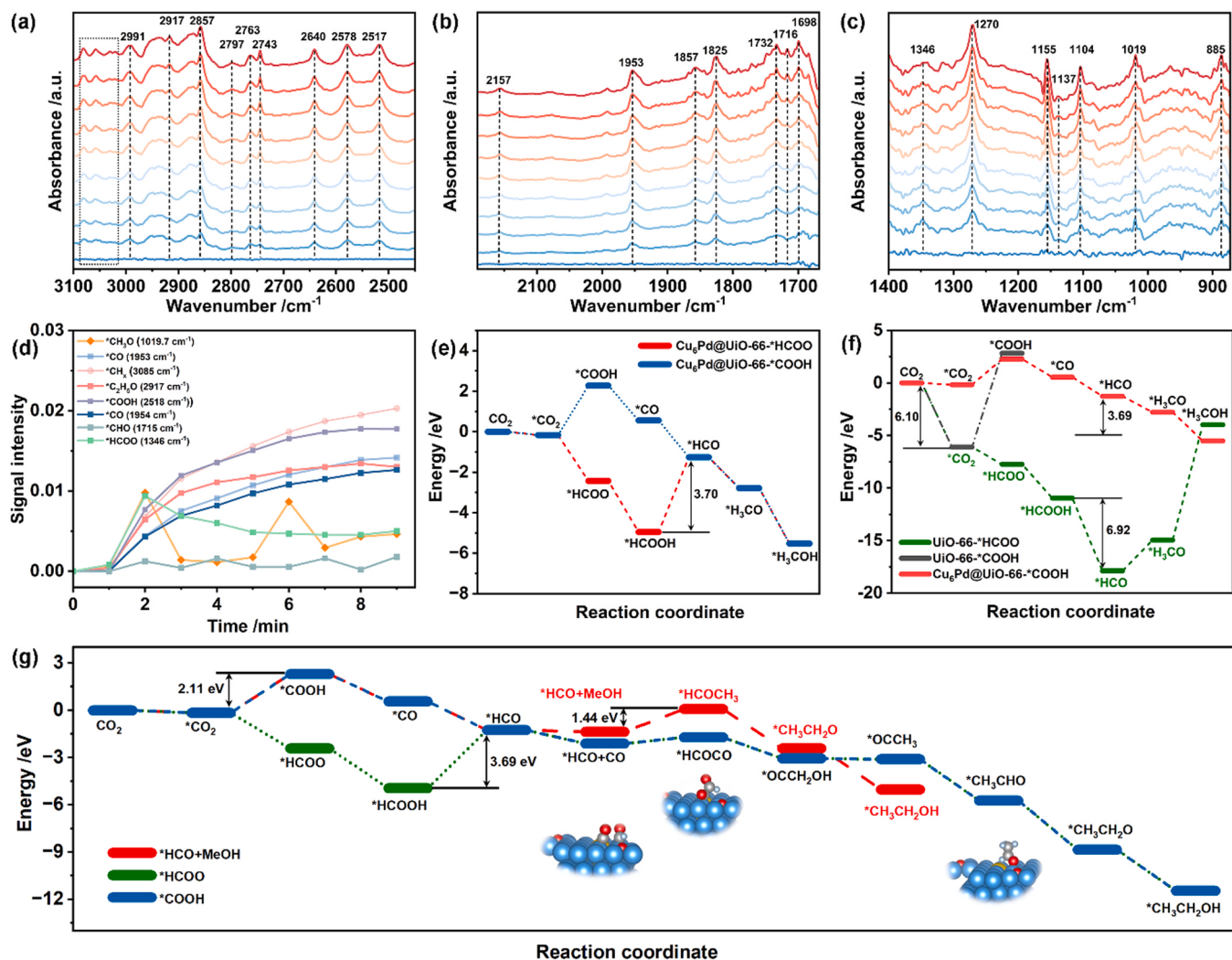


Fig. 5. In-situ DRIFTS spectroscopy of Cu₆Pd@UiO-66 exposed to CO₂/H₂ mixed gas (CO₂:H₂ = 1:3) at 180 °C; (d) Dependences of DRIFTS intensity on time in (a-c); (e and f) DFT-calculated energy diagrams for CO₂ hydrogenation to MeOH over UiO-66 and Cu₆Pd@UiO-66; (g) DFT-calculated energy diagrams of CO₂ hydrogenation to ethanol on Cu₆Pd@UiO-66.

sites around Cu-O, whereas *CO tends to be adsorbed at Cu sites near Pd atoms. After C-C coupling, *HCOCO is mainly adsorbed at Cu sites close to Pd atoms. This situation demonstrates that the electrons transfer between Cu and Pd caused an asymmetry of electrons, which in turn reduces the repulsive force between the intermediates and facilitates the C-C coupling. The following steps (*OCCH₂OH-*OCCH₃-*CH₃CHO-*CH₃CH₂O-*CH₃CH₂OH) (**Scheme 2**) are all exothermic reactions with downhill energy barriers. Overall, Cu-Pd bimetallic-induced electron asymmetric distribution is more conducive to lowering the energy barriers for C-C coupling to promote CO₂ hydrogenation to ethanol.

4. Conclusions

In summary, this study utilized a dual-solvent-sonication method to encapsulate copper and a minor quantity of palladium within the cage structure of UiO-66, resulting in the formation of ultrafine Cu₂O/Cu-Pd cluster composites. These composites were then employed as catalysts for photothermally driven hydrogenation of CO₂-to-ethanol. The photothermal ethanol yield of Cu₆Pd@UiO-66 reached 1077.69 μmol·g_{cat}⁻¹·mL⁻¹ with a selectivity of 94.62%, representing an 11.64-fold increase over the non-illumination, and a 3.11-fold enhancement compared with Cu₆@UiO-66. The high performance of Cu₆Pd@UiO-66 can be attributed to its outstanding photogenerated charge generation

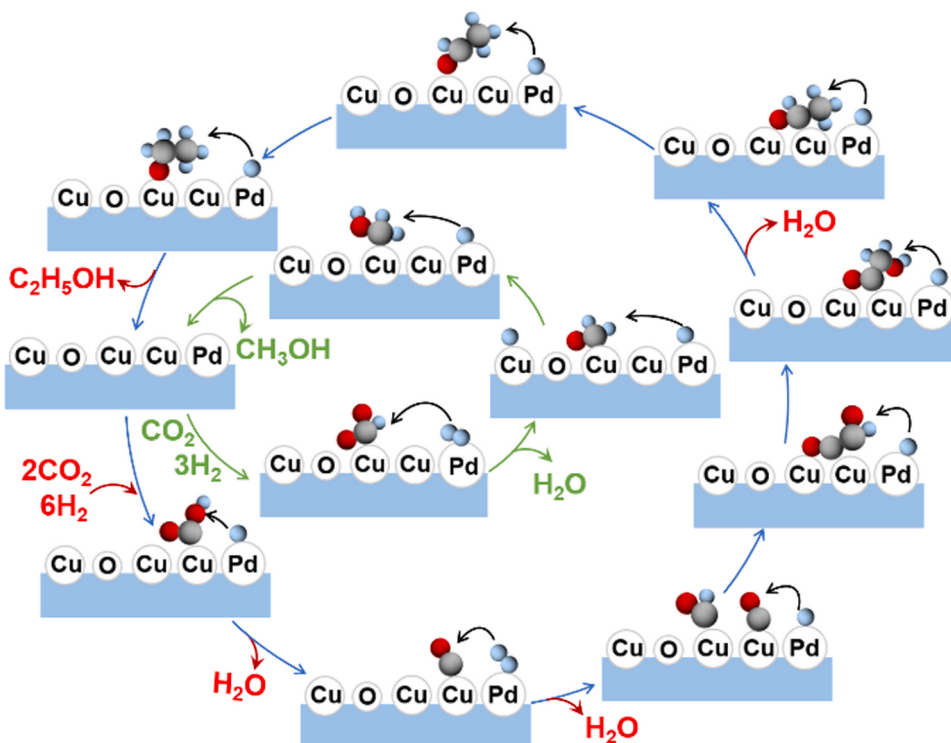
capability and smaller interfacial electrons transfer impedance compared with UiO-66 and Cu₆@UiO-66. The CO-DRIFT results showed that Cu-Cu₂O acted as the active center and has strong CO adsorption ability. The XPS and XAS results disclosed the incorporation of Pd disrupted the original electron distribution, reduced electrostatic repulsion between intermediates, and facilitated the coupling of *CO and *CHO. This study offers evidence supporting the promotion of C-C coupling through an asymmetric electron distribution, potentially advancing the conversion of CO₂ to C₂₊ liquid products.

CRediT authorship contribution statement

Wei Li: Funding acquisition. **Qian Huo:** Data curation. **Qingxin Guan:** Writing – review & editing, Funding acquisition. **Xiaomei Zhou:** Data curation. **Fei Han:** Data curation. **Fu Li:** Writing – review & editing, Writing – original draft, Data curation. **Jingnan Yang:** Conceptualization.

Declaration of Competing Interest

The authors declare no conflict of interest.



Scheme 2. Proposed reaction path for CO_2 hydrogenation over $\text{Cu}_6\text{Pd}@\text{UiO-66}$.

Data Availability

Data will be made available on request.

Acknowledgments

We acknowledge the financial support from the National Natural Science Foundation of China (NSFC 22172082), NCC Fund (NCC2020FH05), and the Fundamental Research Funds for the Central Universities.

Appendix A. Supporting information

Supplementary data associated with this article can be found in the online version at [doi:10.1016/j.apcatb.2024.124187](https://doi.org/10.1016/j.apcatb.2024.124187).

References

- [1] C.D. Thomas, A. Cameron, R.E. Green, M. Bakkenes, L.J. Beaumont, Y. Collingham, B.F.N. Erasmus, M.F. de Siqueira, A. Grainger, L. Hannah, L. Hughes, B. Huntley, A.S. van Jaarsveld, G.F. Midgley, L. Miles, M.A. Ortega-Huerta, A. Townsend Peterson, O.L. Phillips, S.E. Williams, Extinction risk from climate change, *Nature* 427 (2004) 145–148.
- [2] C. Lv, X. Bai, S. Ning, C. Song, Q. Guan, B. Liu, Y. Li, J. Ye, Nanostructured materials for photothermal carbon dioxide hydrogenation: regulating solar utilization and catalytic performance, *ACS Nano* 17 (2023) 1725–1738.
- [3] Z. Yang, Y. Qi, F. Wang, Z. Han, Y. Jiang, H. Han, J. Liu, X. Zhang, W.J. Ong, State-of-the-art advancements in photo-assisted CO_2 hydrogenation: recent progress in catalyst development and reaction mechanisms, *J. Mater. Chem. A* 8 (2020) 24868–24894.
- [4] J. Wu, Y. Huang, W. Ye, Y. Li, CO_2 Reduction: from the electrochemical to photochemical approach, *Adv. Sci.* 4 (2017) 1700194.
- [5] F. Wang, Z. Jin, Y. Jiang, E.H.G. Backus, M. Bonn, S.N. Lou, D. Turchinovich, R. Amal, Probing the charge separation process on $\text{In}_2\text{S}_3/\text{Pt-TiO}_2$ nanocomposites for boosted visible-light photocatalytic hydrogen production, *Appl. Catal. B-Environ.* 198 (2016) 25–31.
- [6] H. Shi, H. Wang, Y. Zhou, J. Li, P. Zhai, X. Li, G.G. Gurzadyan, J. Hou, H. Yang, X. Guo, Atomically dispersed indium-copper dual-metal active sites promoting C-C coupling for CO_2 photoreduction to ethanol, *Angew. Chem. Int. Ed.* 61 (2022) e202208904.
- [7] P. Li, L. Liu, W. An, H. Wang, H. Guo, Y. Liang, W. Cui, Ultrathin porous $\text{g-C}_3\text{N}_4$ nanosheets modified with AuCu alloy nanoparticles and C-C coupling photothermal catalytic reduction of CO_2 to ethanol, *Appl. Catal. B-Environ.* 266 (2020) 118618.
- [8] S. Bai, Q. Shao, P. Wang, Q. Dai, X. Wang, X. Huang, Highly active and selective hydrogenation of CO_2 to ethanol by ordered Pd-Cu nanoparticles, *J. Am. Chem. Soc.* 139 (2017) 6827–6830.
- [9] J.D. Xiao, R. Li, H.-L. Jiang, Metal-organic framework-based photocatalysis for solar fuel production, *Small Methods* 7 (2023) e2201258.
- [10] J. Li, J.-Y. Huang, Y.-X. Meng, L. Li, L.-L. Zhang, H.-L. Jiang, Zr- and Ti-based metal-organic frameworks: synthesis, structures and catalytic applications, *Chem. Commun.* 59 (2023) 2541–2559.
- [11] J.D. Xiao, Q. Shang, Y. Xiong, Q. Zhang, Y. Luo, S.H. Yu, H.-L. Jiang, Boosting photocatalytic hydrogen production of a metal-organic framework decorated with platinum nanoparticles: the platinum location matters, *Angew. Chem. Int. Ed.* 55 (2016) 9389–9393.
- [12] B. An, Z. Li, Y. Song, J. Zhang, L. Zeng, C. Wang, W. Lin, Cooperative copper centres in a metal-organic framework for selective conversion of CO_2 to ethanol, *Nat. Catal.* 2 (2019) 709–717.
- [13] B. Rungtaeweevoranit, J. Baek, J.R. Araujo, B.S. Archanjo, K.M. Choi, O.M. Yaghi, G.A. Somorjai, Copper nanocrystals encapsulated in Zr-based metal-organic frameworks for highly selective CO_2 hydrogenation to methanol, *Nano Lett.* 16 (2016) 7645–7649.
- [14] J. Ye, M. Neurock, D.G. Truhlar, Effect of missing-linker defects on CO_2 hydrogenation to methanol by Cu nanoparticles in UiO-66 , *J. Phys. Chem. C* 126 (2022) 13157–13167.
- [15] T. Liu, X. Hong, G. Liu, In situ generation of the $\text{Cu}@\text{3D-ZrO}_x$ framework catalyst for selective methanol synthesis from CO_2/H_2 , *ACS Catal.* 10 (2019) 93–102.
- [16] L.L. Ling, W. Yang, P. Yan, M. Wang, H.-L. Jiang, Light-assisted CO_2 hydrogenation over $\text{Pd}_3\text{Cu}@\text{UiO-66}$ promoted by active sites in close proximity, *Angew. Chem. Int. Ed.* 61 (2022) e202116396.
- [17] J. Zhang, B. An, Z. Li, Y. Cao, Y. Dai, W. Wang, L. Zeng, W. Lin, C. Wang, Neighboring Zn-Zr sites in a metal-organic framework for CO_2 hydrogenation, *J. Am. Chem. Soc.* 143 (2021) 8829–8837.
- [18] L. Zeng, Z. Wang, Y. Wang, J. Wang, Y. Guo, H. Hu, X. He, C. Wang, W. Lin, Photoactivation of Cu centers in metal-organic frameworks for selective CO_2 conversion to ethanol, *J. Am. Chem. Soc.* 142 (2020) 75–79.
- [19] G. Wang, C.T. He, R. Huang, J. Mao, D. Wang, Y. Li, Photoinduction of Cu single atoms decorated on UiO-66-NH_2 for enhanced photocatalytic reduction of CO_2 to liquid fuels, *J. Am. Chem. Soc.* 142 (2020) 19339–19345.
- [20] B. An, J. Zhang, K. Cheng, P. Ji, C. Wang, W. Lin, Confinement of ultrasmall Cu/ZnO nanoparticles in metal-organic frameworks for selective methanol synthesis from catalytic hydrogenation of CO_2 , *J. Am. Chem. Soc.* 139 (2017) 3834–3840.
- [21] L. Zhao, J. Bian, X. Zhang, L. Bai, L. Xu, Y. Qu, Z. Li, Y. Li, L. Jing, Construction of ultrathin s-scheme heterojunctions of single Ni atom immobilized Ti-MOF and BiVO_4 for CO_2 photoconversion of nearly 100% to CO by pure water, *Adv. Mater.* 34 (2022) e2205303.

[22] X. Liu, J. Chen, P. Liu, H. Zhang, G. Li, T. An, H. Zhao, Controlled growth of CuO/Cu₂O hollow microsphere composites as efficient visible-light-active photocatalysts, *Appl. Catal. A-Gen.* 521 (2016) 34–41.

[23] F. Lan, H. Zhang, C. Zhao, Y. Shu, Q. Guan, W. Li, Copper clusters encapsulated in carbonaceous mesoporous silica nanospheres for the valorization of biomass-derived molecules, *ACS Catal.* 12 (2022) 5711–5725.

[24] Y. Zhu, J. Zheng, J. Ye, Y. Cui, K. Koh, L. Kovarik, D.M. Camaioni, J.L. Fulton, D. G. Truhlar, M. Neurock, C.J. Cramer, O.Y. Gutiérrez, J.A. Lercher, Copper-zirconia interfaces in UiO-66 enable selective catalytic hydrogenation of CO₂ to methanol, *Nat. Commun.* 11 (2020) 5849.

[25] Z. Zhao, J. Huang, P. Liao, X. Chen, Highly efficient electroreduction of CO₂ to ethanol via asymmetric C-C coupling by a metal-organic framework with heterodimetal dual sites, *J. Am. Chem. Soc.* 145 (2023) 26783–26790.

[26] J. Zhu, W. Shao, X. Li, X. Jiao, J. Zhu, Y. Sun, Asymmetric triple-atom sites confined in ternary oxide enabling selective CO₂ photothermal reduction to acetate, *J. Am. Chem. Soc.* 143 (2021) 18233–18241.

[27] S. Liu, C. Yang, S. Zha, D. Sharapa, F. Stoldt, Z.J. Zhao, J. Gong, Moderate surface segregation promotes selective ethanol production in CO₂ hydrogenation reaction over CoCu catalysts, *Angew. Chem. Int. Ed.* 61 (2022) e202109027.

[28] X. Xu, T. Lan, G. Zhao, Q. Nie, F. Jiang, Y. Lu, Interface-hydroxyl enabling methanol steam reforming toward CO-free hydrogen production over inverse ZrO₂/Cu catalyst, *Appl. Catal. B-Environ.* 334 (2023) 122839.

[29] P. Ji, X. Feng, S.S. Veroneau, Y. Song, W. Lin, Trivalent zirconium and hafnium metal-organic frameworks for catalytic 1,4-dearomatative additions of pyridines and quinolines, *J. Am. Chem. Soc.* 139 (2017) 15600–15603.

[30] A.G. Sato, D.P. Volanti, D.M. Meira, S. Damyanova, E. Longo, J.M.C. Bueno, Effect of the ZrO₂ phase on the structure and behavior of supported Cu catalysts for ethanol conversion, *J. Catal.* 307 (2013) 1–17.

[31] Y. Lou, F. Jiang, W. Zhu, L. Wang, T. Yao, S. Wang, B. Yang, B. Yang, Y. Zhu, X. Liu, CeO₂ supported Pd dimers boosting CO₂ hydrogenation to ethanol, *Appl. Catal. B-Environ.* 291 (2021) 120122.

[32] Y. Zhang, L. Cao, G. Bai, X. Lan, Engineering single Cu sites into covalent organic framework for selective photocatalytic CO₂ reduction, *Small* (2023) e2300035.

[33] A.A. Zhang, D. Si, H. Huang, L. Xie, Z.B. Fang, T.F. Liu, R. Cao, Partial metalation of porphyrin moieties in hydrogen-bonded organic frameworks provides enhanced CO₂ photoreduction activity, *Angew. Chem. Int. Ed.* 61 (2022) e202203955.

[34] M. Yang, J. Yu, A. Zimina, B.B. Sarma, J.D. Grunwaldt, H. Zada, L. Wang, J. Sun, Unlocking a dual-channel pathway in CO₂ hydrogenation to methanol over single-site zirconium on amorphous silica, *Angew. Chem. Int. Ed.* (2023) e202312292.

[35] Q. Wu, R. Du, P. Wang, G.I.N. Waterhouse, J. Li, Y. Qiu, K. Yan, Y. Zhao, W.-W. Zhao, H.-J. Tsai, M.-C. Chen, S.-F. Hung, X. Wang, G. Chen, Nanograin-boundary-abundant Cu₂O-Cu nanocubes with high C₂₊ selectivity and good stability during electrochemical CO₂ reduction at a current density of 500 mA/cm², *ACS Nano* 17 (2023) 12884–12894.

[36] X. Ye, C. Yang, X. Pan, J. Ma, Y. Zhang, Y. Ren, X. Liu, L. Li, Y. Huang, Highly selective hydrogenation of CO₂ to ethanol via designed bifunctional Ir₁-In₂O₃ single-atom catalyst, *J. Am. Chem. Soc.* 142 (2020) 19001–19005.

[37] L. Wang, S. He, L. Wang, Y. Lei, X. Meng, F.-S. Xiao, Cobalt-nickel catalysts for selective hydrogenation of carbon dioxide into ethanol, *ACS Catal.* 9 (2019) 11335–11340.

[38] D. Xu, M. Ding, X. Hong, G. Liu, S.C.E. Tsang, Selective C₂₊ Alcohol Synthesis from Direct CO₂ Hydrogenation over a Cs-Promoted Cu-Fe-Zn Catalyst, *ACS Catal.* 10 (2020) 5250–5260.

[39] L. Wang, L. Wang, J. Zhang, X. Liu, H. Wang, W. Zhang, Q. Yang, J. Ma, X. Dong, S. J. Yoo, J.G. Kim, X. Meng, F.S. Xiao, Selective hydrogenation of CO₂ to ethanol over cobalt catalysts, *Angew. Chem. Int. Ed.* 57 (2018) 6104–6108.

[40] K. Zheng, Y. Li, B. Liu, F. Jiang, Y. Xu, X. Liu, Ti-doped CeO₂ stabilized single-atom rhodium catalyst for selective and stable CO₂ hydrogenation to ethanol, *Angew. Chem. Int. Ed.* 61 (2022) e202210991.

[41] Z. He, Q. Qian, J. Ma, Q. Meng, H. Zhou, J. Song, Z. Liu, B. Han, Water-enhanced synthesis of higher alcohols from CO₂ hydrogenation over a Pt/Co₃O₄ catalyst under milder conditions, *Angew. Chem. Int. Ed.* 55 (2015) 737–741.

[42] L. Ding, T. Shi, J. Gu, Y. Cui, Z. Zhang, C. Yang, T. Chen, M. Lin, P. Wang, N. Xue, L. Peng, X. Guo, Y. Zhu, Z. Chen, W. Ding, CO₂ hydrogenation to ethanol over Cu@Na-beta, *Chem* 6 (2020) 2673–2689.

[43] H. Zhang, H. Han, L. Xiao, W. Wu, Highly selective synthesis of ethanol via CO₂ hydrogenation over CoMoCx catalysts, *ChemCatChem* 13 (2021) 3333–3339.

[44] D. Wang, Q. Bi, G. Yin, W. Zhao, F. Huang, X. Xie, M. Jiang, Direct synthesis of ethanol via CO₂ hydrogenation using supported gold catalysts, *Chem. Commun.* 52 (2016) 14226–14229.

[45] E. Gong, S. Ali, C.B. Hiragond, H.S. Kim, N.S. Powar, D. Kim, H. Kim, S.-I. In, Solar fuels: research and development strategies to accelerate photocatalytic CO₂ conversion into hydrocarbon fuels, *Energy Environ. Sci.* 15 (2022) 880–937.

[46] G. Wang, Z. Chen, T. Wang, D. Wang, J. Mao, P and Cu dual sites on graphitic carbon nitride for photocatalytic CO₂ reduction to hydrocarbon fuels with high C₂H₆ evolution, *Angew. Chem. Int. Ed.* 61 (2022) e202210789.

[47] Y. Wang, W. Gao, K. Li, Y. Zheng, Z. Xie, W. Na, J.G. Chen, H. Wang, Strong evidence of the role of H₂O in affecting methanol selectivity from CO₂ hydrogenation over Cu-ZnO-ZrO₂, *Chem* 6 (2020) 419–430.

[48] G. Wang, Y. Wu, Z. Li, Z. Lou, Q. Chen, Y. Li, D. Wang, J. Mao, Engineering a copper single-atom electron bridge to achieve efficient photocatalytic CO₂ conversion, *Angew. Chem. Int. Ed.* (2023) e202218460.

[49] D. Xu, Y. Wang, M. Ding, X. Hong, G. Liu, S.C.E. Tsang, Advances in higher alcohol synthesis from CO₂ hydrogenation, *Chem* 7 (2021) 849–881.